Journal of Solid State Chemistry 182 (2009) 1563–1569

Contents lists available at ScienceDirect

Journal of Solid State Chemistry

journal homepage: www.elsevier.com/locate/jssc

Influence of fuel-to-oxidizer ratio on the magnetic properties of Fe-doped In_2O_3 nanoparticles synthesized by solution combustion method

J. Yu, L.B. Duan, Y.C. Wang, G.H. Rao *

Beijing National Laboratory for Condensed Matter Physics, Institute of Physics, Chinese Academy of Sciences, Beijing 100190, People's Republic of China

ARTICLE INFO

Article history:
Received 12 December 2008
Received in revised form
28 February 2009
Accepted 28 March 2009
Available online 8 April 2009

PACS:
74.62.Bf
81.20.Ka
75.90.+w
85.75.−d

Keywords:
Doped indium trioxide
Combustion synthesis
Crystal structure
Magnetization
Spintronic materials

ABSTRACT

Two series of $(In_{1-x}Fe_x)_2O_3$ were prepared by a solution combustion method using different fuel-to-oxidizer (i.e. glycine/metal nitrate, *G/N*) ratios. The crystal structure and magnetic properties of the compounds were investigated by means of X-ray diffraction, transmission electron microscopy and magnetic measurements. Detailed structural analysis shows the solubility limits of Fe in In_2O_3 are $x = 0.08$ and 0.45 for the *G/N* ratios of 5/4 and 5/6, respectively. Crystallite size of the samples prepared with the *G/N* ratio of 5/6 is much smaller than that of the samples prepared with the *G/N* ratio of 5/4. At room temperature, the sample with $x = 0.01$ prepared with the *G/N* ratio of 5/4 is paramagnetic and those with $x = 0.03$–0.07 are ferromagnetic, whereas the samples with $x = 0.15$–0.45 prepared with the *G/N* ratio of 5/6 show superparamagnetic behavior and those samples with $x < 0.15$ are paramagnetic. Different magnetic behavior of these two series of samples could be attributed to different origins of magnetism. The magnetism of the samples prepared with the *G/N* ratio of 5/4 might originate from the existence of mixed valence Fe ions whereas the magnetism of the samples prepared with the *G/N* ratio of 5/6 could be due to the small crystallite size.

1. Introduction

Diluted magnetic semiconductor (DMS) materials combining magnetic and semiconductor functions are expected to have a wide application prospect in the spintronic devices, which simultaneously exploit the charge and spin properties of electrons [1,2]. Accordingly, the search for room temperature (RT) ferromagnetic DMS materials has been intensively carried out in recent years, and many such materials have been reported. However, it is essential to illuminate the origin of RT ferromagnetism (FM) in these materials, because only intrinsic FM arising from magnetic atoms embedded in nonmagnetic semiconductor lattice can be used in spintronic devices.

Recently, research of transitional metal (TM) doped In_2O_3 is widely concerned. In_2O_3 matrix is a wide-band gap n-type semiconductor ($E_g = 3.75$ eV) as a result of oxygen deficiencies [3,4]. Its carrier density can be tuned by doping Sn or by introducing oxygen deficiencies, and high solubility of TM in In_2O_3 can be achieved, which are desirable for achieving a high Curie temperature above RT.

So far, a lot of research groups have claimed RT FM in TM-doped In_2O_3 or tin-doped In_2O_3 (ITO) (where *TM* = Cr, Mn, Fe, Co, Ni) thin films or powders [5–10]. Fe doped In_2O_3 powders have been studied by several research groups [11,12]. Yoo et al. and Peleckis et al. reported that Fe doped In_2O_3 bulk samples prepared by a conventional solid state synthesis technique showed paramagnetic behavior at RT, whereas RT FM could be achieved in Fe and Cu (or Mn) codoped In_2O_3 bulk samples [13,14]. They confirmed through detailed structural and magnetic analysis that the RT FM in their samples did not result from an impurity phase and could be attributed to the multivalence of Fe ions in the cation lattice. However, Chu et al. failed to observe the RT FM in Fe and Cu codoped In_2O_3 samples prepared by a co-precipitation method [15]. Okada et al. reported RT FM of Fe doped In_2O_3 bulk samples prepared by solid state reaction and attributed it to dispersed Fe_3O_4 nanoparticles in the prepared samples [16]. In addition, some groups argued that the defects in Fe doped In_2O_3 bulk samples were responsible for the presence of RT FM [17,18]. The existing reports show that the origin of the observed FM in Fe-doped In_2O_3 powders remains unclear and also the magnetic properties of the samples seem sensitive to the synthesis methods. Combustion approach has many advantages over other synthesis method. The wet chemical process allows us to control easily the powder characteristics such as crystallite size, surface

* Corresponding author. Fax: +86 1082649531.
E-mail address: ghrao@aphy.iphy.ac.cn (G.H. Rao).

0022-4596/$ - see front matter © 2009 Elsevier Inc. All rights reserved.
doi:10.1016/j.jssc.2009.03.023

area, etc. by governing flame temperature during combustion which is dependent on fuel-to-oxidizer ratio [19]. The change of powder characteristics has a potential effect on its structure and properties. In this paper, we report the synthesis of two series of Fe-doped In_2O_3 samples with the use of different fuel-to-oxidized ratio by solution combustion method to further explore the crystal structure and magnetic properties of Fe-doped In_2O_3 compounds. Detailed analysis shows that the fuel-to-oxidized ratio has a prominent effect on the particle size and magnetic properties of Fe-doped In_2O_3 compounds.

2. Experiment

The compounds with nominal composition $(In_{1-x}Fe_x)_2O_3$ were synthesized by a solution combustion method. An appropriate amount of analytical grade metal nitrate $Fe(NO_3)_3 \cdot 9H_2O$, 1 mol/L solution of $In(NO_3)_3$ and glycine (NH_2CH_2COOH) were dissolved in deionized water to form precursor solution. The precursor solution was concentrated by heating it in a beaker until excess free water was evaporated and spontaneous ignition occurred. The exothermic reaction can generally be expressed as [20]

$$M(NO_3)_3 + (\phi + 2/3)NH_2CH_2COOH + [9/4(\phi - 1)]O_2 \Rightarrow 1/2M_2O_3 + ([3 + (\phi + 2/3)]/2)N_2\uparrow_g + [2(\phi + 2/3)]CO_2\uparrow_g + [5/2(\phi + 2/3)]H_2O\uparrow_g \ (M = In_{1-x}Fe_x)$$

In the above reaction, glycine serves as fuel for the combustion, being oxidized by the nitrate ions. $\phi = 1$ means that the initial mixture does not require atmospheric oxygen for a complete oxidation of fuel, while $\phi > 1$ (< 1) implies fuel-rich (poor) conditions. Two G/N ratios ($G/N = \phi + 2/3 = 5/4$ or 5/6) of fuel-poor condition were used in our experiment to prepare two series of $(In_{1-x}Fe_x)_2O_3$ ($x = 0$–0.1 and $x = 0$–0.45, respectively).

The phase composition and crystal structure of the samples were examined by X-ray powder diffraction (XRD) using a PANalytical X'pert PRO Alpha-1 diffractometer with Cu$K\alpha_1$ radiation ($\lambda = 1.5406$ Å) and high resolution transmission electron microscopy (HRTEM, JEM-2010). The XRD data were analyzed by the Rietveld refinement program FULLPROF [21,22]. X-ray photoelectron spectroscopy (XPS) spectra were recorded on a VG MK II spectrometer at room temperature using an Al$K\alpha$ X-ray source ($hv = 1486.6$ eV) and the binding energy values were measured with respect to C 1s peak at 284.6 eV. Magnetic measurements were performed on a superconducting quantum interference device (SQUID, Quantum Design MPMS 7).

3. Results and discussion

Fig. 1 shows the XRD patterns of the $(In_{1-x}Fe_x)_2O_3$ prepared with the G/N ratio of 5/4. The bottom two rows of vertical bars indicate Bragg reflection positions of In_2O_3 (the upper row) and $InFe_2O_4$ (the lower row). The XRD patterns of the samples doped with Fe up to $x = 0.07$ exhibit only diffraction peaks of the cubic bixbyite In_2O_3 structure (space group: $Ia\bar{3}$) and do not show any evidence of impurity phases. Trace amount of $InFe_2O_4$ as a secondary phase was found in the sample with $x = 0.1$ as marked by the downward arrow in the inset of Fig. 1. The Rietveld refinement results of the XRD patterns for the samples with $x = 0.05$ and 0.1 are shown in Fig. 2. As the amount of Fe doping increases, the XRD peaks shift to higher angle, indicating a decrease of the unit cell parameter. Evolution of cell constant a derived from the Rietveld refinement with the Fe content x is shown in Fig. 3. The cell constant a decreases linearly with x from $x = 0$ to 0.07, which conforms to Vegard's law. Therefore, we conclude that the solubility limit of Fe ions in In_2O_3 under the condition of $G/N = 5/4$ is about $x = 0.08$ and the smaller Fe ions replace the In ions randomly in In_2O_3 for $x < 0.08$.

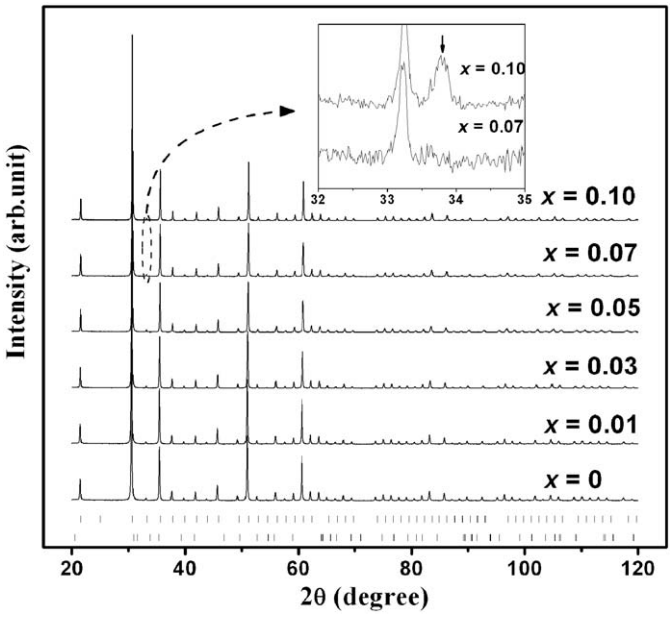

Fig. 1. XRD patterns of $(In_{1-x}Fe_x)_2O_3$ prepared with the G/N ratio of 5/4. Two rows of vertical bars at the bottom indicate the Bragg reflection positions of In_2O_3 (upper row) and $InFe_2O_4$ (lower row). The inset is the zoom-in of XRD patterns for the samples with $x = 0.07$ and 0.10. The downward arrow marks the reflection position of $InFe_2O_4$.

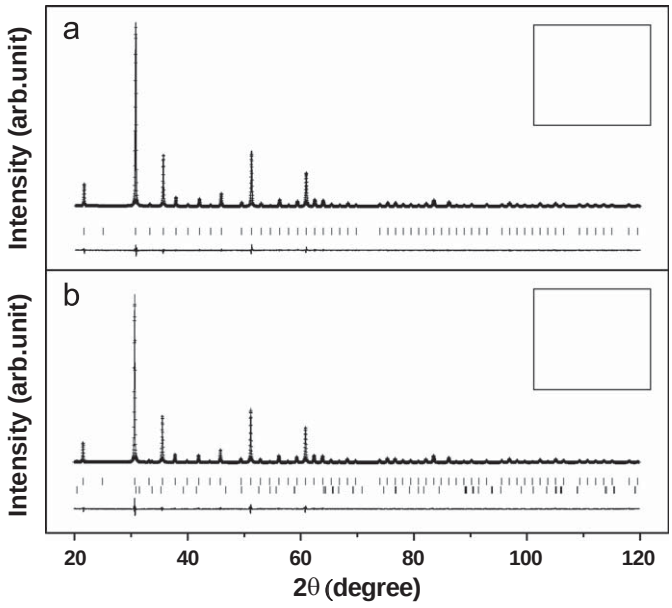

Fig. 2. Observed (solid curve) and calculated (crosses) XRD patterns of $(In_{0.95}Fe_{0.05})_2O_3$ (a) and $(In_{0.9}Fe_{0.1})_2O_3$ prepared with the G/N ratio of 5/4 (b). The vertical bars at the bottom indicate the expected Bragg reflection positions, and the lowest curve is the difference between the observed and the calculated XRD patterns.

Fig. 4 shows the XRD patterns of $(In_{1-x}Fe_x)_2O_3$ prepared with the G/N ratio of 5/6. The XRD patterns indicate all the samples with $x \leqslant 0.35$ are single phase with the cubic bixbyite In_2O_3 structure. Small amount of impurity phase $InFe_2O_4$ was found in the sample with $x = 0.45$. There is a clear shift to higher angle and a broadening of the XRD peaks with increasing Fe doping. Crystallite size calculated from FWHM (full width at half maximum) of the XRD peaks by using Scherrer's equation after

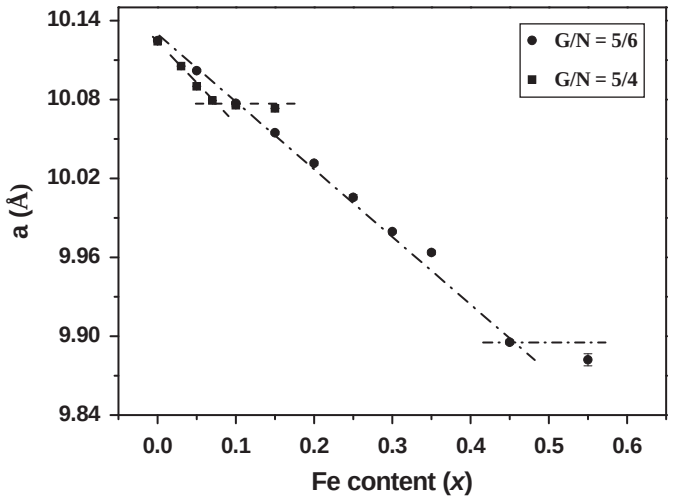

Fig. 3. Evolution of cell constant a of $(In_{1-x}Fe_x)_2O_3$ prepared with the G/N ratios of 5/4 and 5/6 as a function of the Fe content x.

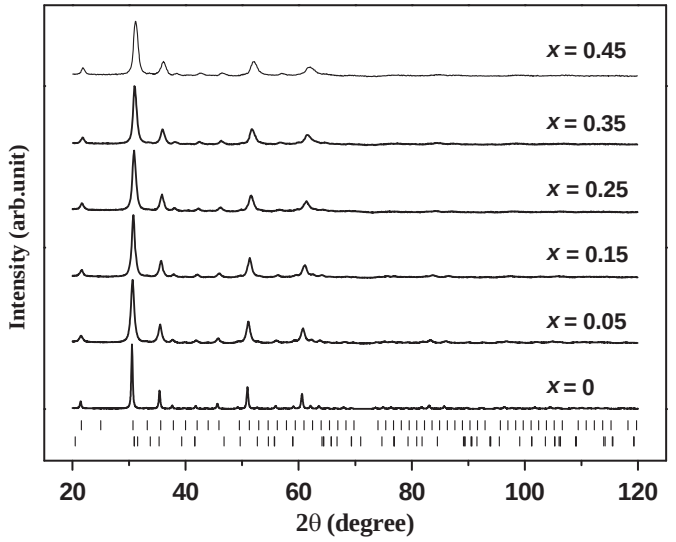

Fig. 4. XRD patterns of $(In_{1-x}Fe_x)_2O_3$ prepared with the G/N ratio of 5/6. Two rows of vertical bars at the bottom indicate the Bragg reflection positions of In_2O_3 (upper row) and $InFe_2O_4$ (lower row).

correction for instrumental broadening using LaB_6 powder as standard sample is about 10–20 nm, which is consistent with TEM analysis (see below). The crystallite size of the samples prepared with the G/N ratio of 5/6 is much smaller than that of the samples prepared with the G/N ratio of 5/4 (about 40–50 nm as estimated from FWHM of the XRD peaks). The Rietveld refinement results of the XRD patterns for the samples with $x = 0.35$ and 0.45 are shown in Fig. 5. Evolution of cell constant a derived from the Rietveld refinement with the Fe content x conforms to Vegard's law (Fig. 3). Therefore, the solubility limit of Fe ions in In_2O_3 under the condition of the G/N ratio of 5/6 is about $x = 0.45$.

Typical TEM images of $(In_{0.95}Fe_{0.05})_2O_3$ prepared with the G/N ratios 5/4 and 5/6 are shown in Fig. 6(a)–(e), respectively. Low resolution TEM images in Fig. 6(a) and (c) show that particle size of the sample prepared with the G/N ratio of 5/4 is about 50 nm, much bigger than that of the sample prepared with the G/N ratio of 5/6 (about 20 nm). HRTEM analyses were carried out on different regions of both the samples. The images reveal no segregation of secondary phases and a uniform microstructure. A spacing of $(1\bar{1}2)$ planes in $(In_{0.95}Fe_{0.05})_2O_3$ prepared with the G/N ratio of 5/4 is about 4.12 Å as indicated in Fig. 6(b). The bottom inset shows the selected area fast Fourier transform (FFT) pattern. A spacing of $(\bar{2}2\bar{2})$ planes in $(In_{0.95}Fe_{0.05})_2O_3$ prepared with the G/N ratio of 5/6 is about 2.92 Å as indicated in Fig. 6(e). The top-left inset shows the selected area FFT pattern.

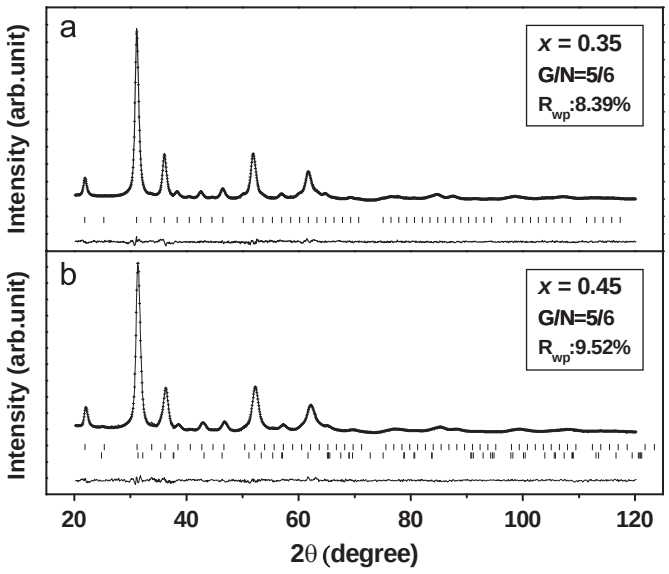

Fig. 5. Observed (solid curve) and calculated (crosses) XRD patterns of $(In_{0.8}Fe_{0.2})_2O_3$ (a) and $(In_{0.65}Fe_{0.35})_2O_3$ prepared with the G/N ratio of 5/6 (b). The vertical bars at the bottom indicate the expected Bragg reflection positions, and the lowest curve is the difference between the observed and the calculated XRD patterns.

It can be concluded from above structural and microscopic analyses that the change of the G/N ratio in the solution combustion reaction has a prominent effect on the solubility limit of Fe ions in In_2O_3, cell parameters and crystallite size of the $(In_{1-x}Fe_x)_2O_3$ compounds. Slightly decrease of the G/N ratio makes the solubility limit of Fe ions in In_2O_3 increases from about 8% to 45%. The solution combustion reaction method is a nonequilibrium synthesis approach by which we could produce supersaturated solid solution due to well mixing of the reactants at the atomic level and to the instantly high temperature when the reaction occurs. Crystallite size of the samples prepared with the G/N ratio of 5/4 is much bigger than that of the samples with the G/N ratio of 5/6 probably because of the higher reaction temperature of the former [20]. The solubility limit of the samples prepared with the G/N ratio of 5/4 is much lower than that of the samples prepared with the G/N ratio of 5/6. The reason could be that more glycine used as fuel might induce a valence reduction from Fe^{3+} to Fe^{2+}, which is beneficial to the formation of the secondary phase $InFe_2O_4$. Besides, the valence reduction of Fe ions is probably also a reason for the smaller cell parameters of the sample prepared with the G/N ratio of 5/4 than that of the sample prepared with the G/N ratio of 5/6, taking into account that the Fe^{2+}–O bond length of unit valence ($R_0 = 1.734$ Å) is smaller than that of Fe^{3+}–O ($R_0 = 1.759$ Å) [23].

Fig. 7 shows XPS spectra of the Fe2p in $(In_{0.95}Fe_{0.05})_2O_3$ prepared with the G/N ratio of 5/4 and in $(In_{0.65}Fe_{0.35})_2O_3$ prepared with the G/N ratio of 5/6. The binding energy of the Fe $2p_{3/2}$ for $(In_{0.65}Fe_{0.35})_2O_3$ prepared with the G/N ratios 5/6 is 711 eV (Fig. 7(b)) which is consistent with the Fe $2p_{3/2}$ peak for Fe^{3+} [5,24]. A clear broadening and shift to lower binding energy of the Fe $2p_{3/2}$ peak for $(In_{0.95}Fe_{0.05})_2O_3$ prepared with the G/N ratio of 5/4 are indicative of the mixing of Fe^{2+} and Fe^{3+} ions or of the mixed valence for the Fe ions [25].

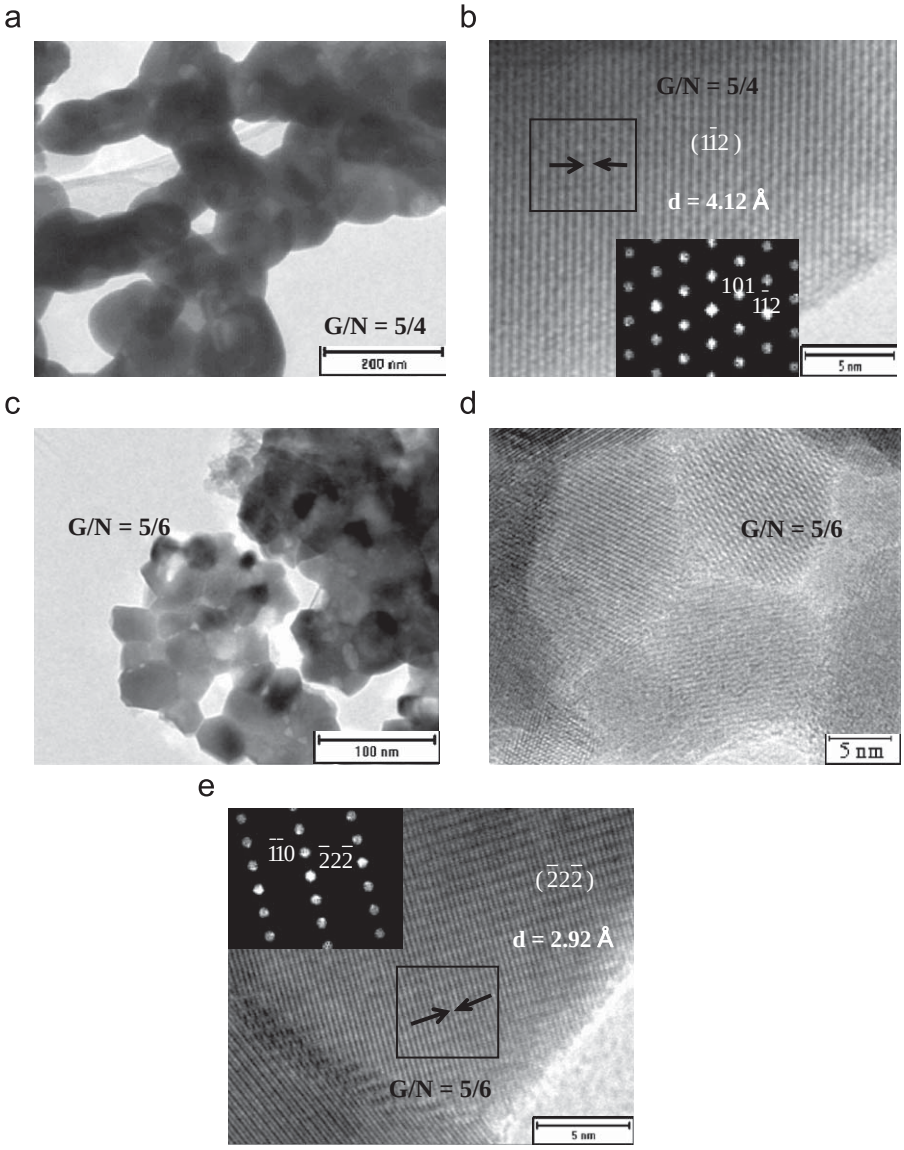

Fig. 6. TEM images of $(In_{0.95}Fe_{0.05})_2O_3$ prepared with the *G/N* ratio of 5/4 (a, b) and with the *G/N* ratio of 5/6 (c–e).

Magnetization (M) at 300 K of the $(In_{1-x}Fe_x)_2O_3$ prepared with the *G/N* ratio of 5/4 as a function of magnetic field (H) up to 5000 Oe is shown in Fig. 8. All the samples, except for the sample with $x = 0.01$, are ferromagnetic with a coercive field of about 120 Oe at RT (inset in Fig. 8). The sample with $x = 0.01$ is paramagnetic at RT due to nearly isolated Fe ions. The saturation magnetization value M_S increases with the Fe concentration x, implying increased number of Fe ions participating in the FM interaction. It is interesting that the coercive field is almost unchanged with the Fe concentration x, the reason of which is unclear.

Fig. 9 shows zero field cooling and field cooling (ZFC/FC) magnetization curves in a field of 200 Oe of the $(In_{0.95}Fe_{0.05})_2O_3$ prepared with the *G/N* ratio of 5/4. The ZFC/FC curves could be used as a reliable technique to indirectly detect any ultrasmall magnetic nanoclusters in the matrix, which could not be easily detected by usual characterization techniques such as XRD, XPS and TEM and normally display a superparamagnetic behavior with a low blocking temperature (T_B) [26]. The absence of T_B in our samples indicates no tiny ferromagnetic nanoclusters. In addition, the secondary phase $InFe_2O_4$ exhibits ferrimagnetic behavior below Curie temperature ($T_C = 250$ K) in the samples and can be excluded from the origin of the RT FM [27]. Therefore, we believe the RT FM of the $(In_{0.95}Fe_{0.05})_2O_3$ prepared with the *G/N* ratio of 5/4 is an intrinsic property arising from Fe ions incorporation into the lattice of indium oxide. There is a slight discrepancy between ZFC and FC curves due to the FM imbedded in the paramagnetic matrix [28], which is also indicated by the unsaturated M–H curve at 300 K in Fig. 8.

Magnetization (M) at 300 K of the $(In_{1-x}Fe_x)_2O_3$ with $x =$ 0-0.45 prepared with the *G/N* ratio of 5/6 as a function of magnetic field (H) up to 4100 Oe is shown in Fig. 10. Magnetization for the samples with $x < 0.15$ increases almost linearly with the applied field, indicating these samples are paramagnetic at RT. Evident ferromagnetic behavior appears when Fe doping concentration reaches $x > 0.10$ (Fig. 10(a)). Fig. 10(b) shows magnetic hysteresis loops for the samples with $x = 0.2$ and 0.35 at 5 and 300 K. The top-left inset and bottom-right inset are the zoom-in of the loops, respectively. The coercive fields at RT of the sample is very small (about 10 Oe) but the coercive field at 5 K is increased to about

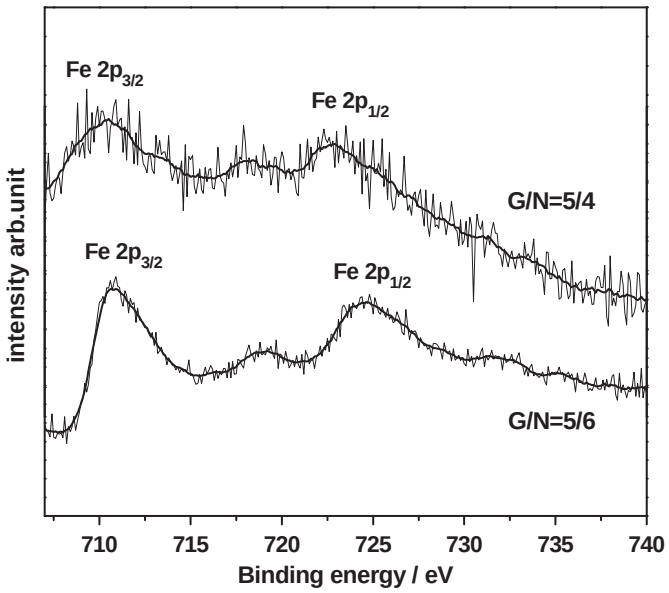

Fig. 7. XPS spectra of the Fe2p in $(In_{0.95}Fe_{0.05})_2O_3$ prepared with the *G/N* ratio of 5/6 and in $(In_{0.65}Fe_{0.35})_2O_3$ prepared with the *G/N* ratio of 5/4.

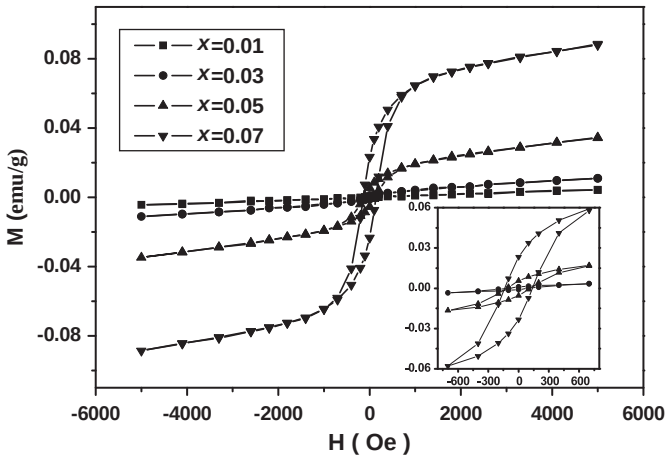

Fig. 8. *M* vs *H* curves of $(In_{1-x}Fe_x)_2O_3$ prepared with the *G/N* ratio of 5/4 at 300 K. The inset is the zoom-in of *M–H* curves for the samples with $x = 0.03$, 0.05 and 0.07.

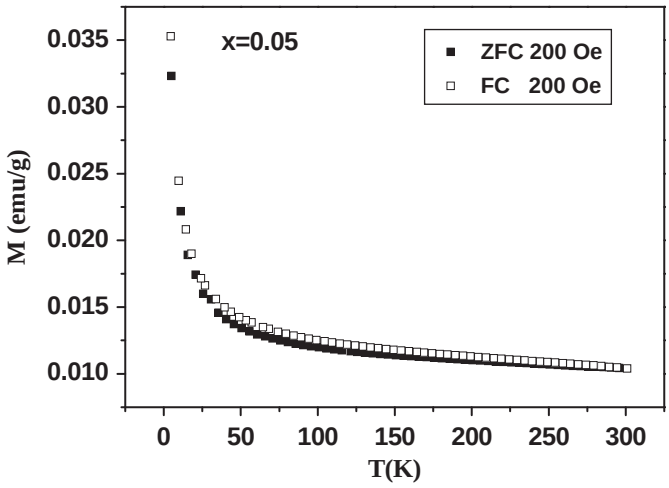

Fig. 9. *M* vs *T* curves of $(In_{0.95}Fe_{0.05})_2O_3$ prepared with the *G/N* ratio of 5/4 in a field of 200 Oe after cooling in zero field and in the field of 200 Oe, respectively.

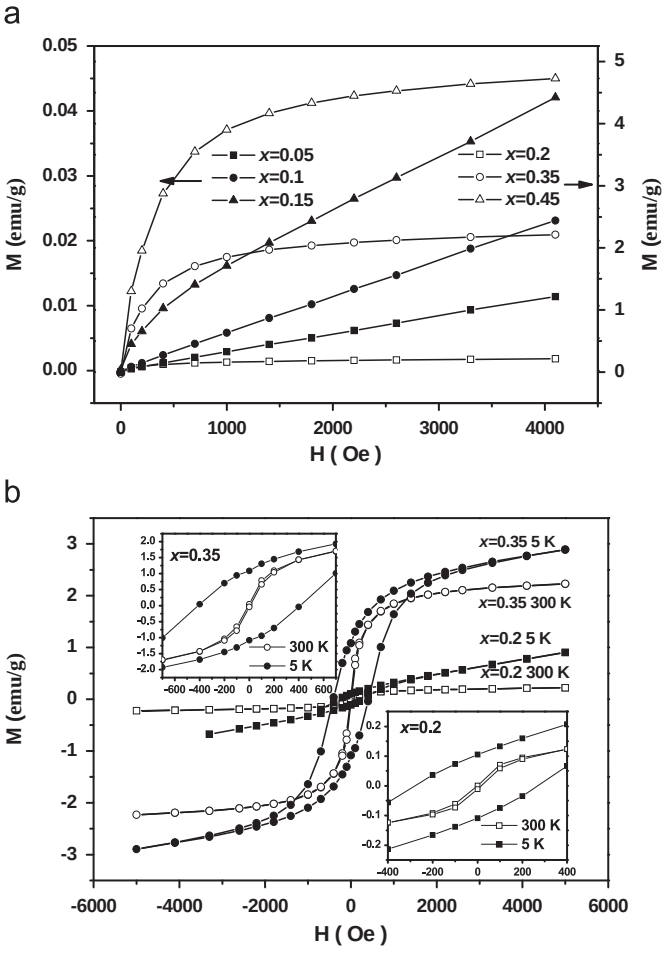

Fig. 10. (a) *M* vs *H* curves of $(In_{1-x}Fe_x)_2O_3$ prepared with the *G/N* ratio of 5/6 at 300 K. (b) The hysteresis loops of $(In_{1-x}Fe_x)_2O_3$ with $x = 0.2$ and 0.35 at 300 and 5 K. The top-left inset is the zoom-in of the *M–H* curve for the sample with $x = 0.35$. The bottom-right inset is the zoom-in of the *M–H* curve for the sample with $x = 0.2$.

250 Oe for the sample with $x = 0.2$ and to about 400 Oe for $x = 0.35$, which suggests that the samples probably are superparamagnetic.

Fig. 11(a) shows plots of magnetization and inverse susceptibility $1/\chi$ as functions of temperature for $(In_{0.95}Fe_{0.05})_2O_3$ prepared with the *G/N* ratio of 5/6 on warming in a field of 1000 Oe after cooling in zero field. The high temperature part between 200 and 300 K of $1/\chi$ vs. *T* displays Curie–Weiss behavior and the data can be fitted by the Curie–Weiss law, $\chi = C_0x/(T+\Theta)$ [29]. The effective magnetic moment μ_{eff} and the effective spin angular momentum *S* are derived by: $\mu_{eff} = [3k_BC_0x/N_A]^{-1/2} = g[S(S+1)]^{1/2}\mu_B$, where *g* is the Landé factor and for transition metal ions it is reasonable to take $g = 2$ [29]. The derived values of μ_{eff} and *S* are 5.85 μ_B and 2.47, which are comparable to the values for a high-spin Fe^{3+} ion ($S = 5/2$, $\mu = 5.4$–$5.96\,\mu_B$ [30]). Fig. 11(b) shows the ZFC/FC magnetization curves of $(In_{0.8}Fe_{0.2})_2O_3$ in a field of 200 Oe. Fig. 11(d) shows the ZFC/FC magnetization curves of $(In_{0.65}Fe_{0.35})_2O_3$ in a field of 300 Oe. An irreversible behavior is observed on the ZFC/FC curves of both the samples, which indicates these samples are superparamagnetic in agreement with the increased coercive field at low temperature (inset in Fig. 10(b)). The superparamagnetism (SPM) could arise from small crystallite size. T_B of both the samples is close to RT. There is no indication of Verwey transition of Fe_3O_4 nanoparticles on the ZFC/FC curves, suggesting that there should be no tiny Fe_3O_4 nanoclusters. In addition, the SPM disappears under a field of

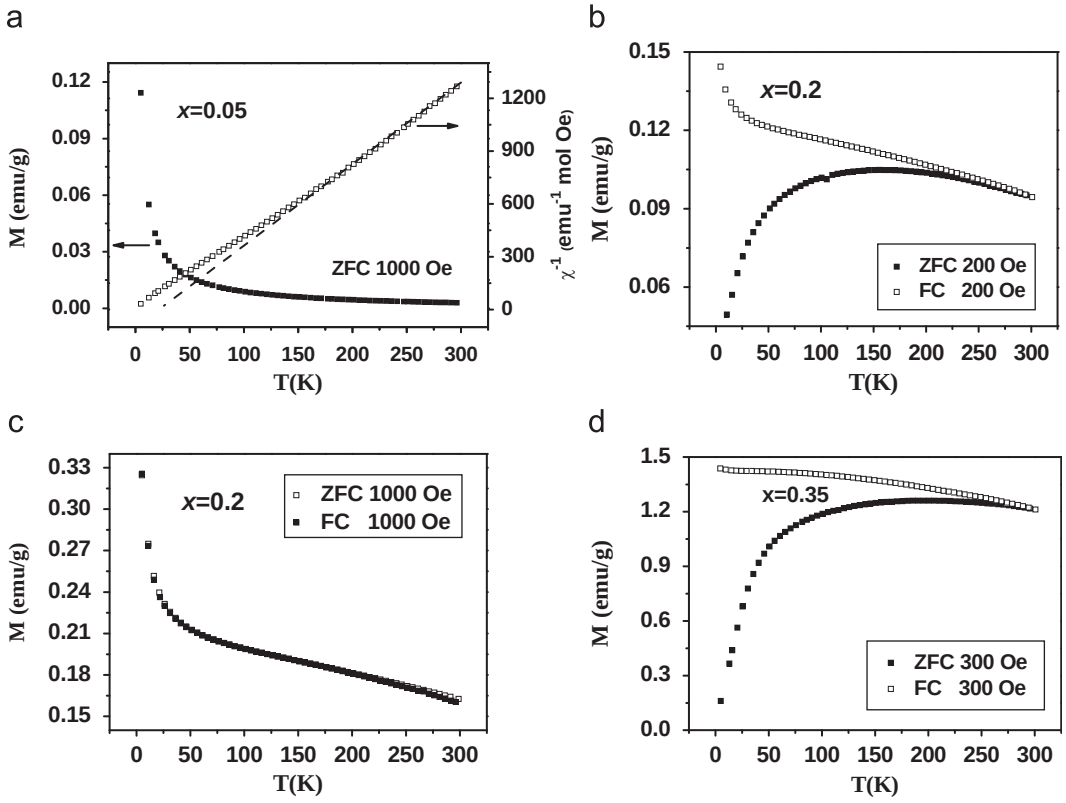

Fig. 11. (a) M vs T curves of $(In_{0.95}Fe_{0.05})_2O_3$ prepared with the G/N ratio of 5/6 in a field of 1000 Oe after cooling in zero field. The dashed lines are the theoretical fits to the Curie–Weiss law. (b) ZFC/FC curves of $(In_{0.8}Fe_{0.2})_2O_3$ in fields of 200 Oe and (c) 1000 Oe. (d) ZFC/FC curves of $(In_{0.65}Fe_{0.35})_2O_3$ in a field of 300 Oe.

1000 Oe (Fig. 11c) which is different from the temperature dependence of magnetization of possible γ-Fe_2O_3 nanoparticles on warming in a field of 1000 Oe [31,32]. Therefore, the SPM is an intrinsic property of Fe incorporation into the In_2O_3 matrix.

The above magnetic measurements show that magnetic properties of two series of samples prepared with different G/N ratios have a remarkable difference, suggesting that they have different origins of magnetism. For the samples prepared with the G/N ratio of 5/4, its RT FM probably originates from the existence of mixed valence Fe ions, whereas the RT SPM of the samples prepared with the G/N ratio of 5/6 can be attributed to the small crystallite size.

4. Conclusion

We have synthesized two series of $(In_{1-x}Fe_x)_2O_3$ with the use of two different G/N ratios (5/4 and 5/6, respectively) by a solution combustion method. The crystal structure and magnetic properties of these two kinds of Fe doped samples have been investigated and compared. The solubility limit of Fe in In_2O_3 prepared with the G/N ratio of 5/4 is about $x = 0.08$ and that of the samples prepared with the G/N ratio of 5/6 is about $x = 0.45$. The higher combustion reaction temperature with the G/N ratio of 5/4 leads to larger crystallite size of the samples. Magnetic measurements show that the sample with $x = 0.01$ prepared with the G/N ratio of 5/4 is paramagnetic at RT and the samples with $x =$ 0.03–0.07 exhibit RT FM, while the samples with $x = 0.15$–0.45 prepared with the G/N ratio of 5/6 show SPM at RT. Different magnetic behavior of these two series of samples could be attributed to the different magnetism origins. The RT FM of the samples with $x = 0.03$–0.07 prepared with the G/N ratio of 5/4 could originate from the existence of the mixed valence Fe ions in the samples, whereas the RT SPM of the samples with $x = 0.15$–0.45 prepared with the G/N ratio of 5/6 results from the small crystallite size.

Acknowledgment

This work is supported by National Natural Science Foundation of China (Grant no. 50572118).

References

[1] T. Dietl, H. Ohno, F. Matsukura, J. Cibert, D. Ferrand, Science 287 (2000) 1019.
[2] J. Philip, N. Theodoropoulou, G. Berera, J.S. Moodera, B. Satpati, Appl. Phys. Lett. 85 (2004) 777.
[3] S.J. Pearton, C.R. Abernathy, M.E. Overberg, G.T. Thaler, D.P. Norton, Y.D. Park, F. Ren, J. Kim, L.A. Boatner, J. Appl. Phys. 93 (2003) 1.
[4] J. Philip, A. Punnoose, B.I. Kim, K.M. Reddy, S. Layne, J.O. Holmes, B. Satpati, P.R. LeClair, T.S. Santos, J.S. Moodera, Nat. Mater. 5 (2006) 298.
[5] P.F. Xing, Y.X. Chen, S.S. Yan, G.L. Liu, L.M. Mei, K. Wang, X.D. Han, Z. Zhang, Appl. Phys. Lett. 92 (2008) 022513.
[6] H.S. Kim, S.H. Ji, H. Kim, S.K. Hong, D. Kim, Y.E. Ihm, W.K. Choo, Solid State Commun. 137 (2006) 41.
[7] G. Peleckis, X.L. Wang, S.X. Dou, Appl. Phys. Lett. 89 (2006) 022501.
[8] N.H. Hong, J. Sakai, N.T. Huong, V. Brizé, J. Magn. Magn. Mater. 302 (2006) 228.
[9] D.W. Chu, Y.P. Zeng, D.L. Jiang, Z.M. Ren, Appl. Phys. Lett. 91 (2007) 262503.
[10] N.H. Hong, J. Magn. Magn. Mater. 303 (2006) 338.
[11] S. Kohiki, M. Sasaki, Y. Murakawa, K. Hori, K. Okada, H. Shimooka, T. Tajiri, H. Deguchi, S. Matsushima, M. Oku, T. Shishido, M. Arai, M. Mitome, Y. Bando, Thin Solid Films 505 (2006) 122.
[12] X. Li, C.T. Xia, G.Q. Pei, X.L. He, J. Phys. Chem. Solids 68 (2007) 1836.
[13] Y.K. Yoo, Q.Z. Xue, H.C. Lee, S.F. Cheng, X.D. Xiang, G.F. Dionne, S. Xu, J. He, Y.S. Chu, S.D. Preite, S.E. Lofland, I. Takeuchi, Appl. Phys. Lett. 86 (2005) 042506.
[14] G. Peleckis, X.L. Wang, S.X. Dou, Appl. Phys. Lett. 88 (2006) 132507.
[15] D.W. Chu, Y.P. Zeng, D.L. Jiang, Appl. Phys. Lett. 92 (2008) 182507.
[16] K. Okada, S. Kohiki, S. Nishi, H. Shimooka, H. Deguchi, M. Mitome, Y. Bando, T. Shishido, Jpn. J. Appl. Phys. 46 (2007) L823.

[17] O.D. Jayakumar, I.K. Gopalakrishnan, S.K. Kulshreshtha, A. Gupta, K.V. Rao, D.V. Louzguine-Luzgin, A. Inoue, P.-A. Glans, J.-H. Guo, K. Samanta, M.K. Singh, R.S. Katiyar, Appl. Phys. Lett. 91 (2007) 052504.
[18] S.J. Hu, S.S. Yan, X.L. Lin, X.X. Yao, Y.X. Chen, G.L. Liu, L.M. Mei, Appl. Phys. Lett. 91 (2007) 262514.
[19] R.D. Purohit, B.P. Sharma, K.T. Pillai, A.K. Tyagi, Mater. Res. Bull. 36 (2001) 2711.
[20] K. Deshpande, A. Mukasyan, A. Varma, Chem. Mater. 16 (2004) 4896.
[21] R.A. Young, D.B. Wiles, J. Appl. Cryst. 15 (1982) 430.
[22] J. Rodroguez-Carvajal, Physica B 192 (1993) 55.
[23] I.D. Brown, A. Altermatt, Acta Cryst. B 41 (1985) 244.
[24] P. Graat, M.A.J. Somers, Surf. Interface Anal. 26 (1998) 773.
[25] Y. Gao, S.A. Chambers, J. Cryst. Growth 174 (1997) 446.
[26] X.F. Wang, J.B. Xu, W.Y. Cheung, J. An, N. Ke, Appl. Phys. Lett. 90 (2007) 212502.
[27] K. Oka, M. Azuma, Y. Narumi, K. Kindo, N. Hayashi, Y. Shimakawa, M. Takano, J. Jpn. Soc. Powder Powder Metall. 54 (2007) 53.
[28] L.B. Duan, G.H. Rao, J. Yu, Y.C. Wang, Solid State Commun. 145 (2008) 525.
[29] J. Spałek, A. Lewicki, Z. Tarnawski, J.K. Furdyna, P.R. Galazka, Z. Obuszko, Phys. Rev. B 33 (1986) 3407.
[30] C. Kittel, Introduction to Solid State Physics, seventh ed., Wiley, Singapore, 2004, p. 426.
[31] R. Sappey, E. Vincent, N. Hadacek, F. Chaput, J.P. Boilot, D. Zins, Phys. Rev. B 56 (1997) 14551.
[32] S.S. Guzman, L. Lara, O.P. Camacho, O.R. Fernandez, A. Olivas, R. Escudero, Polymer 48 (2007) 720.